

# High resolution contrast-enhanced microCT reveals the true three-dimensional morphology of the murine placenta

Katrien De Clercq<sup>1</sup>, Eleonora Persoons<sup>1</sup>, Tina Napsó<sup>2</sup>, Catherine Luyten<sup>1</sup>, Tatjana Parac-Vogt<sup>3</sup>, Amanda Sferruzzi-Perri<sup>2</sup>, Greet Kerckhofs<sup>3</sup>, Joris Vriens<sup>3</sup>

<sup>1</sup>KULeuven, <sup>2</sup>University of Cambridge, <sup>3</sup>University of Leuven

Submitted to Proceedings of the National Academy of Sciences of the United States of America

Genetic engineering of the mouse genome identified many genes that are essential for embryogenesis. Remarkably, the prevalence of concomitant placental defects in embryonic lethal mutants is highly underestimated and indicates the importance of detailed placental analysis when phenotyping new individual gene knockouts. Here, we introduce high-resolution contrast-enhanced micro-focus computed tomography (CE-CT) as a non-destructive, high-throughput technique to evaluate the 3D placental morphology. Using a novel contrast agent, Zirconium-substituted Keggin poly-oxometalate (Zr-POM), the soft tissue of the placenta (i.e. different layers and cell types, and its vasculature) was imaged with a resolution of 3.5µm voxel size. This novel approach allowed us to visualize and study early and late stages of placental development. Moreover, CE-CT provides a method to precisely quantify placental parameters (i.e. volumes, volume fraction, ratio of different placental layers and volumes of specific cell populations) that are crucial for statistical comparison studies. The CE-CT assessment of the 3D morphology of the placentas was validated (i) by comparison to standard histological studies, (ii) by evaluating placentas from two different mouse strains, 129S and C57BL/6J mice and (iii) by confirming the placental phenotype of mice lacking phosphoinositol 3-kinase (PI3K)-p110α. Finally, the Zr-POM-based CE-CT allowed for inspection of the vasculature structure in the entire placenta, as well as detecting placental defects in pathologies characterised by embryonic resorption and placental fusion. Taken together, Zr-POM-based CE-CT offers a novel quantitative 3D methodology to investigate placental development or pathologies.

murine placental development | poly-oxometalate-based contrast-enhanced microCT | 3D morphological assessment | placental defects

## INTRODUCTION

The laboratory mouse remains the superior model to assess gene function in embryogenesis. Up to one-third of individual gene knockouts results in fetal demise and thus non-viable offspring (1, 2). Unfortunately, the contribution of placental defects in lethal strains is often disregarded, resulting in the misinterpretation of gene function in the developing embryo. Recently, a systematic phenotyping effort of extraembryonic tissues revealed that placental abnormalities are highly prevalent in lethal or sub-viable mouse mutants, and implies that defects in placentation have been highly underestimated (3, 4). In addition, increasing evidence suggests that improper placental functioning and subsequent intrauterine growth restriction can increase the susceptibility for metabolic diseases such as type-2 diabetes and hypertension (5, 6). Moreover, placental phenotypes are often concomitant with defects within the embryo, including neuronal and vascular development, emphasizing the importance of including the analysis of the placenta when embryonic or perinatal lethality is observed.

The placenta is an extraordinary, albeit transient organ that functions as a surrogate fetal lung, kidney and gut. Hence, defects in the proper formation of this extraembryonic tissue can result

in early embryonic lethality. Moreover, the placenta produces and secretes a variety of hormones to adapt the maternal metabolism in order to comply with the needs of the growing conceptus (7). Murine placentation commences during implantation, around embryonic day 4 (E4), with the formation of the extraembryonic lineages. After chorioallantoic fusion at E8.5, branching morphogenesis is initiated and by E12.5, feto-maternal exchange is established as evidenced by the presence of maternal blood in the placental labyrinth at this stage. The mature murine placenta consist of three clearly distinguishable layers, i.e. the labyrinth, the junctional zone and the maternal decidua (8). The labyrinth is the innermost and largest layer in which the juxtaposition of the maternal and fetal circulation allows an optimal exchange of nutrients and gas over the interhaemal membrane. The junctional zone comprises spongiotrophoblast and glycogen cells and fulfils important metabolic and endocrine functions. This layer is separated from the maternal decidua by a layer of secondary trophoblast giant cells. The maternal decidua is the sole layer that is derived from maternal tissues and is important for providing nutrition during early developmental stages. Interestingly, the relative size and appearance of these layers changes throughout gestation to support fetal needs. As such, the relative size of the labyrinth increases and its structure becomes more complex to allow the exponential growth of the fetus towards term. In contrast, the size of the junctional zone obtained its maximum at the beginning of the third semester and gradually decreases thereafter (9, 10).

## Significance

During pregnancy, the placenta functions as the fetal lung, kidney and gut. Proper placental functioning is therefore paramount during embryonic development. Indeed, placental defects are highly prevalent in mouse mutants showing embryonic death. Here, we validate a new contrast agent that allows development of the intact placenta to be visualized using microCT. This technique enables an initial 3D inspection of the overall placental structure and provides the possibility to quantify different compartments in the placental. Moreover, the non-destructive nature of this contrast agent permits further histological processing of the same sample when defects are observed.

## Reserved for Publication Footnotes

137  
138  
139  
140  
141  
142  
143  
144  
145  
146  
147  
148  
149  
150  
151  
152  
153  
154  
155  
156  
157  
158  
159  
160  
161  
162  
163  
164  
165  
166  
167  
168  
169  
170  
171  
172  
173  
174  
175  
176  
177  
178  
179  
180  
181  
182  
183  
184  
185  
186  
187  
188  
189  
190  
191  
192  
193  
194  
195  
196  
197  
198  
199  
200  
201  
202  
203  
204

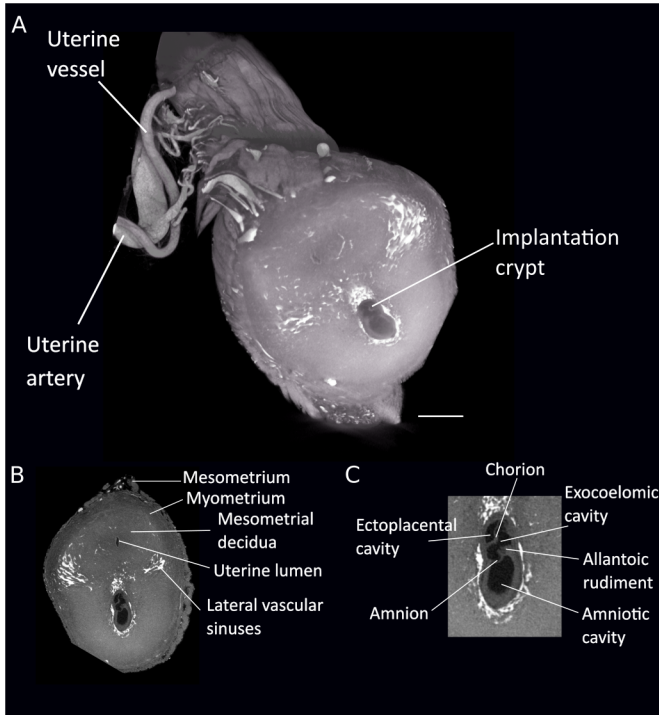


**Fig. 1. Visualization of early implantation site (E7.5).** (A) Zr-POM-based CE-CT 3D rendering on an early implantation site at E7.5. The uterine vasculature can be recognized including the uterine artery, accompanied by the uterine vein that splits into the arcuate artery and then ramifies into the radial arteries and subsequently the spiral arteries. (B) CE-CT image of a cross section of the uterine wall allows the visualization of the typical features of a primitive streak embryo (Theiler stage 11) including the mesometrium, myometrium, endometrium, uterine lumen, vascular sinuses. (C) Magnification of the implanting embryo with the ectoplacental, exocoelomic and amniotic cavity, the chorion, the amnion and the allantois. Scale bar = 500  $\mu$ m. Samples obtained from 12956 mice.

Defects in the formation of either of the placental layers can result in placental insufficiency and thus adversely affect fetal development. Determining the size of the different layers during placentation is therefore considered as a first important step when phenotyping new mutant models. Conventionally, these measurements are assessed by standard histological protocols (11), complemented with additional histologic stains to classify cellular tissue composition. Although this technique has proven to be a valuable tool owing to its high discriminative power and accuracy at cellular level, it is subjected to sampling bias. Due to the complex architecture of the placenta, histological examinations also require a multitude of sections to be analysed before results can be conclusive. Moreover, tissue shrinkage is inherent to embedding procedures and limits the assessment of the correct volume measures. Random sampling and statistical algorithms used in stereology offer an elegant solution to generate 3D quantities from 2D histological sections (12, 13), and has been successfully used in the field of human and murine placentology (9, 14). To date, the process of exhausting sectioning remains the basis for exploring embryonic and placental development and allows for detailed investigations when combined with protein or RNA expression studies. However, it is labour-intensive and time-consuming when morphological information about gross placental morphology is required. Therefore, the field of placental phenotyping would benefit from novel techniques that allow a fast and accurate inspection of the overall placental structure.

Microfocus computed X-ray tomography (microCT) is a recent technique that allows 3D quantification of mineralized

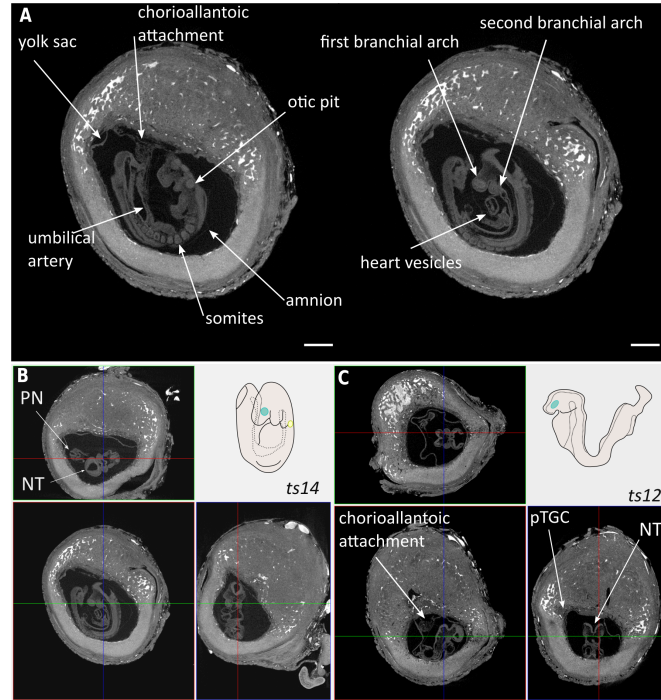


**Fig. 2. Imaging and staging of E9.5 embryo.** (A) CE-CT cross sections showing typical features of E9.5 including chorioallantoic attachment and the presence of the umbilical artery, 12-15 somites, formation of the otic pit, the presence of the first and the second branchial arch and the initiation of heart formation. Scale bar = 500 $\mu$ m. (B, C) Staging E9.5 embryos by 3D histology of CE-CT dataset giving coronal (upper panel), trans axial (lower left panel) and sagittal (lower right panel) sections of the process of embryonic folding in uncompromised (B) and compromised (C) embryonic development, compared to schematic representation of Theiler stage 14 (B, upper right panel) and Theiler stage 12 (C, upper right panel). Samples obtained from 12956 mice. pTGC= primary trophoblast giant cell, PN = posterior neuropore, NT = neural tube.

samples with high contrast and high resolution, though without sample destruction (15, 16). Moreover, it is an established method for vasculature analysis and blood flow modelling by the perfusion of intravascular contrast agents (17). As such, previous studies have used this technique to identify the fetoplacental vasculature of rodents and humans by injecting the contrast agent into the vessels of the umbilical cord (18-23). Additionally, the human fetoplacental vasculature was imaged by 3D microCT by exploiting vascular casting techniques (24). Recently, the interest in contrast-enhanced microCT (CE-CT) has increased as it can also be used to visualize soft tissues, such as muscles and adipocytes, by incubating whole tissue samples in contrast agents (25). This approach was successfully used to visualize the developing embryo using an iodine based contrast agent (26). However, the morphology of extraembryonic tissues has so far not been assessed. Therefore, we aimed to determine whether CE-CT could be extended for the 3D morphological assessment of developing placentas. Polyoxometalate (POM) - based contrast agents have previously been used to visualize the soft tissues surrounding bone, such as adipose tissue and blood vessels, without tissue destruction (27). Here, we used Zirconium-substituted Keggin polyoxometalate (Zr-POM), which has a similar binding efficiency to collagen type I, type II, fibrin and rat tendon as the previously reported Hf-POM (27). These findings indicate that Zr-POM does not alter the chemical structure of these proteins, which is an important advantage compared to the conventional contrast agents, e.g. phosphotungstic acid (PTA) or iodine-based contrast agents such as Lugol (28).

205  
206  
207  
208  
209  
210  
211  
212  
213  
214  
215  
216  
217  
218  
219  
220  
221  
222  
223  
224  
225  
226  
227  
228  
229  
230  
231  
232  
233  
234  
235  
236  
237  
238  
239  
240  
241  
242  
243  
244  
245  
246  
247  
248  
249  
250  
251  
252  
253  
254  
255  
256  
257  
258  
259  
260  
261  
262  
263  
264  
265  
266  
267  
268  
269  
270  
271  
272

273  
274  
275  
276  
277  
278  
279  
280  
281  
282  
283  
284  
285  
286  
287  
288  
289  
290  
291  
292  
293  
294  
295  
296  
297  
298  
299  
300  
301  
302  
303  
304  
305  
306  
307  
308  
309  
310  
311  
312  
313  
314  
315  
316  
317  
318  
319  
320  
321  
322  
323  
324  
325  
326  
327  
328  
329  
330  
331  
332  
333  
334  
335  
336  
337  
338  
339  
340

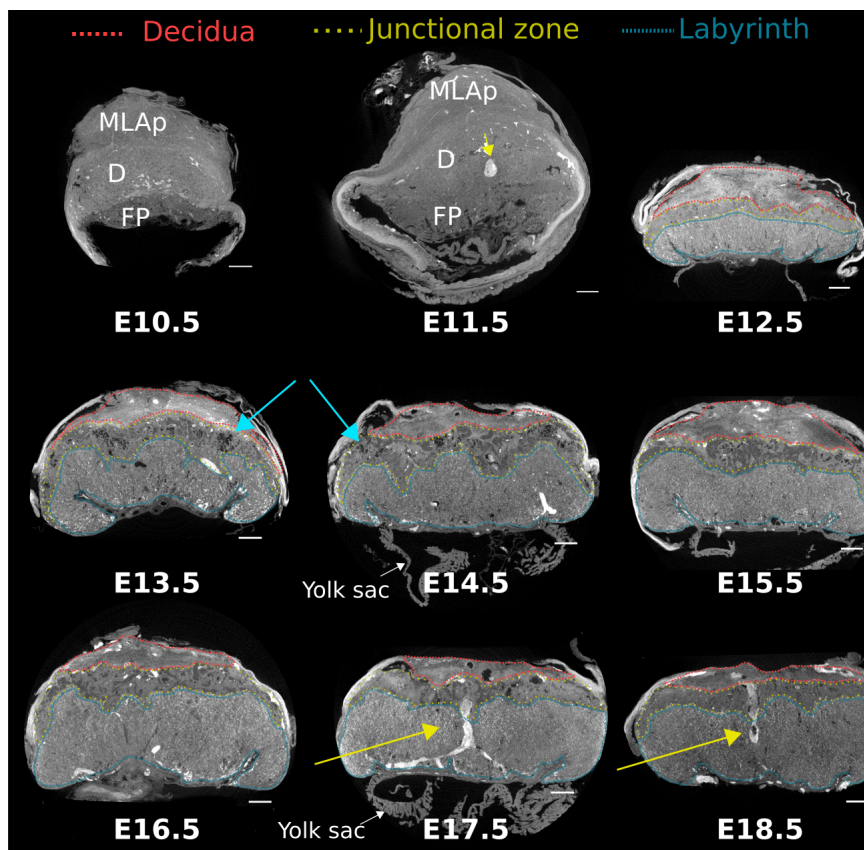


**Fig. 3. Cross-sectional CE-CT images from E10.5-E18.5 placentas, with the different layers indicated.** MLAp = Mesometrial lymphoid aggregate of pregnancy, D = decidua (red), FP = fetal placenta, JZ = junctional zone (yellow), L = labyrinth (blue), blue arrow = lacunae in junctional zone, yellow arrow = maternal canal. Scale bar = 500  $\mu$ m. Samples obtained from 129S6 mice.

Using Zr-POM with CE-CT, we evaluated whether we could 1) visualize the early stages of embryonic and placental development, 2) imaging the morphological structure of the definitive murine placenta, including its three layers, using standard histological staining techniques as a reference, 3) precisely quantify the volumes of placental layers, 4) confirm earlier reported placental morphologies of two mouse strains (129S and C57BL/6J) (29) and of phosphoinositol 3-kinase (PI3K) mutants (30), 5) investigate the vasculature in the intact placenta and 6) study placental pathologies like embryo resorption and placental fusion.

## RESULTS

### 1. Visualization of early placental development

To visualize the early stages of embryonic and placental development, the entire uterine horn was isolated at different time points during early gestation and incubated by Zr-POM. At E 7.5, the typical features of the late primitive streak embryo were distinguishable (Fig. 1). The amniotic cavity was subdivided into three cavities, *i.e.* the ectoplacental, exocoelomic and amniotic cavity. Moreover, elongation of the allantoic bud, starting at the amnion towards the chorion was observed. These hallmarks were suggestive for Theiler stage 11 of the mouse development (31). Interestingly, the use of Zr-POM-based CE-CT allowed us to distinguish the mesometrium, myometrium, the decidua, the uterine lumen surrounded by a single layer of epithelial cells and vascular sinuses in the uterine horn.

At E8.5, an unturned embryo was observed in which neural folding did not initiate yet (SI Appendix, Fig. S1 and Video S1). Moreover, primary trophoblast giant cells surrounding the embryo could be visualised. In this sample, at least 4 somites were detected and the allantois contacted the chorion, suggesting that the embryo is at the end of Theiler stage 12.

At E9.5, embryo turning and chorioallantoic attachment could be investigated (Fig. 2 and SI Appendix Video S2). In Fig. 2A (2D view) and B (3D histology), a certain degree of closure of the neural fold was detected to form the posterior and anterior neuropore. Moreover, the forelimb bud and the 2<sup>nd</sup> branchial arch were visible. Furthermore, the first steps in heart development could be distinguished by the detection of primitive blood vessels. As such, we observed an almost completed turned embryo with 15 somite pairs, indicating that embryo development was at Theiler stage 14. In contrast, embryonic development from a littermate was seemingly arrested at the end of Theiler stage 12 (Fig. 2C). Although chorioallantoic attachment occurred, embryo turning did not ensue since the neural fold was still facing the centre of the implantation crypt, the yolk sac did not occupy the complete amniotic cavity, the second branchial arch was absent and somites were not readily detectable. Altogether, these analyses showed the potency of the Zr-POM-based CE-CT to visualize the hallmarks of early embryonic and placental development.

### 2. Visualization of the mature placenta and validation by histology

In the placenta at E10.5-E11.5, the structures of the definitive chorioallantoic placenta started to become evident. However, the labyrinth could not be distinguished from the junctional zone at these gestational ages using Zr-POM-based CE-CT (Fig. 3). Nevertheless, a clear demarcation between the fetal placenta and the maternal decidua with the mesometrial lymphoid aggregate of pregnancy (MLAp) was apparent.

From E12.5 onwards, the specific morphological features of the placenta became more obvious, allowing the discrimination of different placental layers, of which the appearance and size drastically changed over time (Fig. 3 and SI Appendix Video S3). To confirm the identity of morphological structures observed in

341  
342  
343  
344  
345  
346  
347  
348  
349  
350  
351  
352  
353  
354  
355  
356  
357  
358  
359  
360  
361  
362  
363  
364  
365  
366  
367  
368  
369  
370  
371  
372  
373  
374  
375  
376  
377  
378  
379  
380  
381  
382  
383  
384  
385  
386  
387  
388  
389  
390  
391  
392  
393  
394  
395  
396  
397  
398  
399  
400  
401  
402  
403  
404  
405  
406  
407  
408

409  
410  
411  
412  
413  
414  
415  
416  
417  
418  
419  
420  
421  
422  
423  
424  
425  
426  
427  
428  
429  
430  
431  
432  
433  
434  
435  
436  
437  
438  
439  
440  
441  
442  
443  
444  
445  
446  
447  
448  
449  
450  
451  
452  
453  
454  
455  
456  
457  
458  
459  
460  
461  
462  
463  
464  
465  
466  
467  
468  
469  
470  
471  
472  
473  
474  
475  
476

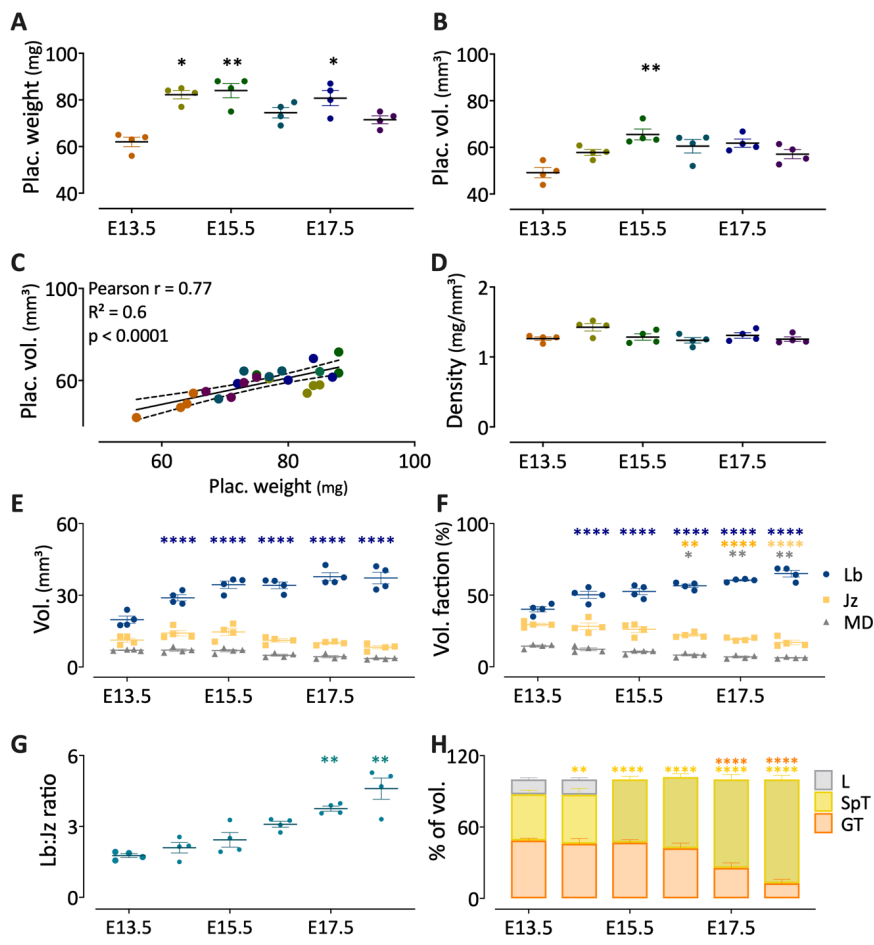


**Fig. 4. Quantification of placental parameters of 129S6 mice through gestation.** (A) Placental weight throughout pregnancy. (B) Placental volume assessed with Zr-POM-based CE-CT. (C) Correlation between weight and volume, Pearson correlation test. (D) Placental density, calculated as placental weight per placental volume, throughout gestation. Volume (E) and volume fraction (F) of the placental layers on different days of gestation. (G) Labyrinth:junctional zone (Lb:Jz) ratio through gestation (arbitrary units) (H) CE-CT-based 3D analysis of the proportion of lacunae (L), glycogen cells (GT) and spongiotrophoblasts (SpT) in the junctional zone throughout gestation. Data are shown as mean  $\pm$  SEM \*  $p < 0.05$ , \*\*  $p < 0.01$ , \*\*\*  $p < 0.001$  Kruskal-Wallis with Dunn's multiple testing correction compared to E13.5 for A-G, Two-Way ANOVA adjusted with Dunnett's multiple testing correction compared to E13.5 for H. N= 4 samples from 3-4 litters per gestational day.

477  
478  
479  
480  
481  
482  
483  
484  
485  
486  
487  
488  
489  
490  
491  
492  
493  
494  
495  
496  
497  
498  
499  
500  
501  
502  
503  
504  
505  
506  
507  
508  
509  
510  
511  
512  
513  
514  
515  
516  
517  
518  
519  
520  
521  
522  
523  
524  
525  
526  
527  
528  
529  
530  
531  
532  
533  
534  
535  
536  
537  
538  
539  
540  
541  
542  
543  
544

CE-CT images, samples from E14.5 and E18.5 that were formerly incubated with Zr-POM, were further processed for immunohistology. In line with previous findings (32), Zr-POM did not interfere with subsequent stains, nor did it affect the specificity (Appendix Fig. S2 and S3A), providing the possibility of a one-on-one comparison. Notably, the difference in cellular composition between the placental layers was sufficient to readily distinguish the gross placental morphology on CE-CT images. At E14.5, the maternal decidua consists of decidualized stromal cells and uterine NK cells, which are glycogen positive but negative for cytokeratin. The junctional zone mainly comprises spongiotrophoblast and glycogen trophoblast cells. The former are densely packed cells while the latter are highly vacuolated cells with few organelles that grow in rounded islets (33). Interestingly, this substantial difference in cellular composition made it possible to discriminate these cell populations in CE-CT images, which was confirmed on the corresponding PAS stained section (SI Appendix Fig. S3B). Interestingly, isolated inclusions of the junctional zone into the labyrinth, containing both glycogen and spongiotrophoblast cells, could be observed with Zr-POM-based CE-CT (SI Appendix Fig. S3A, yellow arrow)(34). Markedly, comparing CE-CT images with histology revealed a high affinity of Zr-POM for blood. This advantage enabled the tracking of spiral arteries that diverge into maternal canals, which branch near the chorionic plate (Fig. 3, yellow arrows and SI Appendix Video S3). In addition, maternal veins that transverse the junctional zone to drain the maternal blood into venous sinuses (SI Appendix Fig. S3B, arrowheads), provided a helpful landmark to delineate the boundaries between the junctional zone and the decidua.

A strong correlation between the 2D labyrinth area quantified on histological sections and the area quantified on the corresponding CE-CT images, proved that specific regions can be easily distinguished on CE-CT images (Spearman correlation coefficient 0.83,  $R^2 = 0.67$ ,  $p < 0.01$ , Fig. S4). The ratio of the labyrinth area to junctional zone area (Lb:Jz ratio) is a measure that is used to indicate the composition of the placenta. However, 360° sectioning around the midline using CE-CT based 3D histology revealed substantial differences in placental structures in different sections. To exemplify, the Lb:Jz ratio was determined in E16.5 placentas of littermates on sections containing a maternal canal, an indication of a midline sections (35, 36). Notably, 2D Lb:Jz ratio of perpendicular sections (sagittal and transaxial) with the same maternal canal present were markedly different (4.3 vs. 2.4 at location 1 and 3.2 vs. 2.3 in location 2) (SI Appendix Fig. S3C). In contrast, differences between sagittal and transaxial sections were less variable in a littermate, even though these sections were further away from the middle of the placenta and from each other (3.1 vs. 3.0 in location 1 and 4.3 vs. 3.3 in location 2) (SI Appendix Fig. S3D). Given the substantial variation in placental structure between sections (SI Appendix Video S3), quantification of placental regions would benefit from whole organ 3D measurements and encouraged us to quantify the volumes of the different placental layers.

### 3. Quantification of the mature placenta by Zr-POM-based CE-CT

The placental 3D volume was precisely quantified using Zr-POM-based CE-CT without the need for extensive sectioning. Fluctuations in 3D placental volumes during gestation were similar to placental weights recorded immediately following dissec-

545  
546  
547  
548  
549  
550  
551  
552  
553  
554  
555  
556  
557  
558  
559  
560  
561  
562  
563  
564  
565  
566  
567  
568  
569  
570  
571  
572  
573  
574  
575  
576  
577  
578  
579  
580  
581  
582  
583  
584  
585  
586  
587  
588  
589  
590  
591  
592  
593  
594  
595  
596  
597  
598  
599  
600  
601  
602  
603  
604  
605  
606  
607  
608  
609  
610  
611  
612

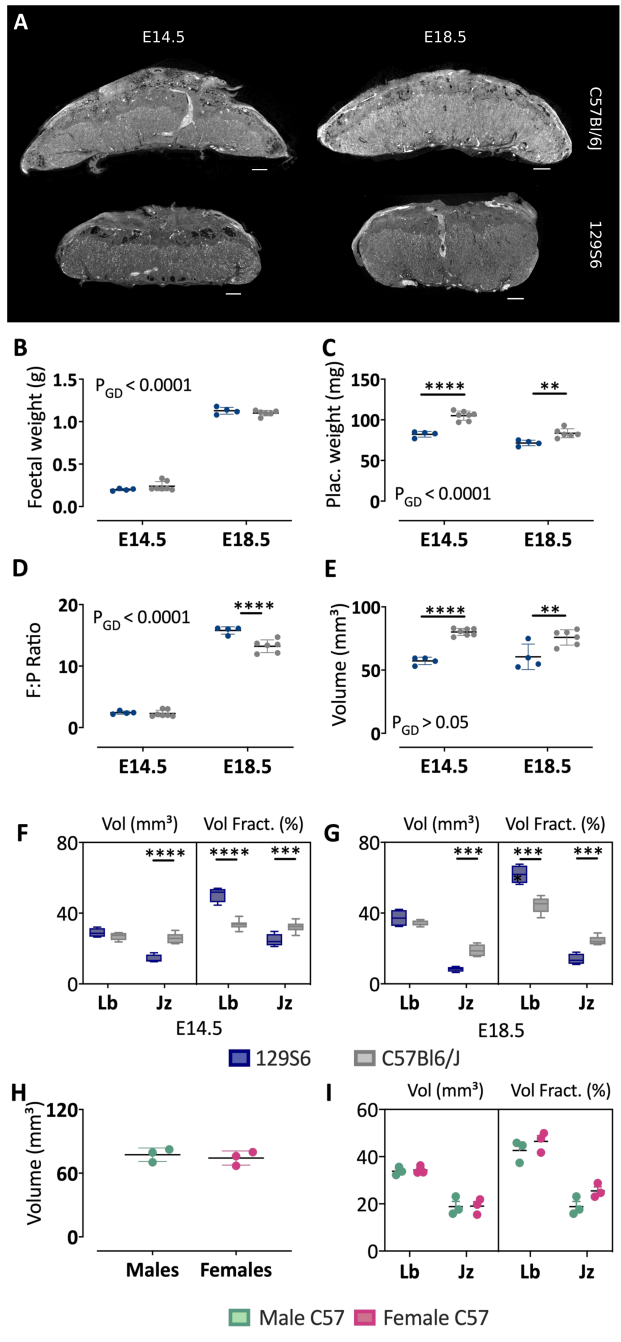


**Fig. 5. Morphometric comparison of C57BL/6J and 129S6 placentas using Zr-POM-based CE-CT.** (A) Representative CE-CT image of a placenta isolated at E14.5 and E18.5 from C57BL/6J and 129S6 mice. Scale bar = 500  $\mu$ m. Fetal weight (B), placental weight (C), placental efficiency as fetal: placental weight (F:P) ratios (D) and placental volume (E) at E14.5 and E18.5. Volume and the volume fraction of the junctional zone (Jz) and labyrinth (Lb) at E14.5 (F) and 18.5 (G). (H) Placental volumes of male versus female placentas from C57BL/6J mice at E18.5. (I) Volume and volume fraction of junctional zone and labyrinth in male versus female placentas. Statistical comparison with Two-way Anova adjusted with Sidak's multiple comparison test (A-G and I) or Mann-Whitney test (H). \*  $p < 0.05$ , \*\*  $p < 0.01$ , \*\*\*\*  $p < 0.0001$ .  $P_{GD}$  = p-value for the effect of the gestational day. Jz = junctional zone, Lb = labyrinth, N= 4 129S6 placentas from 3 litters and N = 6-7 C57BL/6J placentas from 3 litters per gestational day.

tion (Fig. 4A-B and SI Appendix Table S1). This resulted in a strong correlation between placental weight and 3D volume

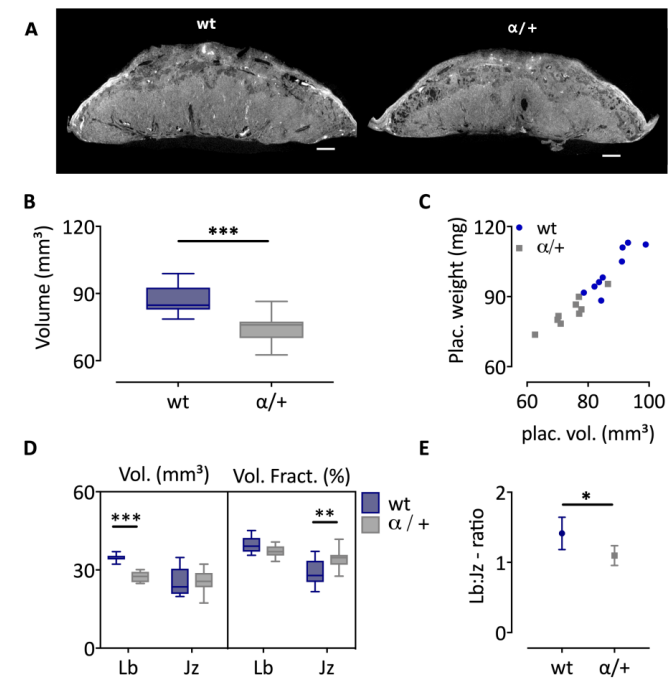


**Fig. 6. Morphometric comparison of wt and PI3K  $\alpha^{+/+}$  mutants at E16.** (A) Representative CE-CT image of a placenta from wt and  $\alpha^{+/+}$  littermates. Scale bar = 500  $\mu$ m. (B) Placental volume determined by CE-CT, Unpaired T-test. (C) Correlation between placental weight and volume. (D) Volume and the volume fraction of the junctional zone (Jz) and labyrinth (Lb), Two-way Anova adjusted with Sidak's multiple comparison test. (E) Lb:Jz ratio shown as mean  $\pm$  95% coincidence interval, Unpaired T-test. N= 9 samples from 5 litters/group. \*  $p < 0.05$ , \*\*  $p < 0.01$ , \*\*\*  $p < 0.001$ , Jz = junctional zone, Lb = labyrinth.

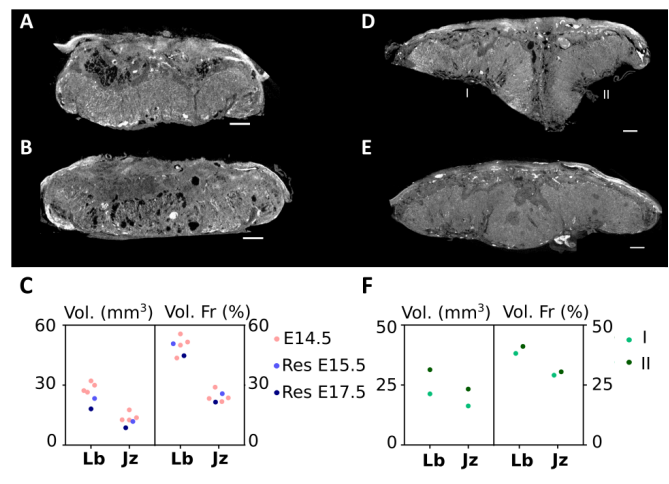


**Fig. 7. Visualization and quantification of biological variances in placenta.** (A) CE-CT cross section of the placenta isolated from a resorbed 129S6 embryo at E15.5. (B) CE-CT cross section of the placenta isolated from a resorbed 129S6 embryo at E17.5. (C) Quantification of the absolute volume and the volume fraction of the placentas (labyrinth (Lb) and junctional zone (Jz)) from resorbed embryos, compared to the characteristics of an E14.5 placenta. (D) CE-CT cross section of a fused placenta from a C57BL/6J mouse at E18.5. (E) CE-CT cross section of a twin placenta from a C57BL/6J mouse at E18.5. (F) Quantification of the absolute volume and the volume fraction of the two parts of the fused placentas. Scale bar = 500 $\mu$ m

(Pearson correlation coefficient 0.77,  $R^2=0.6$ ,  $p < 0.001$ , Fig. 4C). The volumetric mass density of the placentas was calculated as

613  
614  
615  
616  
617  
618  
619  
620  
621  
622  
623  
624  
625  
626  
627  
628  
629  
630  
631  
632  
633  
634  
635  
636  
637  
638  
639  
640  
641  
642  
643  
644  
645  
646  
647  
648  
649  
650  
651  
652  
653  
654  
655  
656  
657  
658  
659  
660  
661  
662  
663  
664  
665  
666  
667  
668  
669  
670  
671  
672  
673  
674  
675  
676  
677  
678  
679  
680

weight per volume, but did not show significant alterations over time. Nevertheless, a subtle difference at E14.5 was observed as placental weight increased by 32%, whereas placental volume increased by 17% between E13.5 and E14.5 (Fig. 4D). Altogether, Zr-POM-based CE-CT allowed for a fast and reliable quantification of placental volume and density.

Given the accuracy of Zr-POM-based CE-CT to discriminate the different placental layers, the volume and volume fractions of the different layers were determined throughout gestation (Fig. 4E and F, SI Appendix Table S2). In line with literature (9), the volume and volume fraction of the maternal decidua drastically decreased towards term, from  $7.1 \pm 0.3 \text{ mm}^3$  to  $3.5 \pm 0.4 \text{ mm}^3$ , relating to  $14.4 \pm 4.8\%$  and  $5.9 \pm 0.8\%$  respectively. In contrast, the volume and volume fraction of the labyrinth significantly increased daily, indicating its continuous growth and development. As such, the absolute labyrinth volume almost doubled ( $19.7 \pm 3.1 \text{ mm}^3$  at E13.5 to  $37.2 \pm 4.7 \text{ mm}^3$  at E18.5), and was reflected in a significant increase in volume fraction from  $40.1 \pm 2.2\%$  to  $61.8 \pm 5.1\%$  of the placenta, respectively. Instead, the volume of the junctional zone reached its maximum at E15.5 ( $11.3 \pm 1.8 \text{ mm}^3$  at E13.5 until  $14.7 \pm 3.2 \text{ mm}^3$  at E15.5), whereas the volume fraction of the junctional zone peaked at E14.5 ( $22.8 \pm 3.5\%$  to  $24.7 \pm 1.7\%$ ). Thereafter, volume fraction significantly decreased towards term, probably because of the massive migration of glycogen cells into the decidua prior to term ( $8.3 \pm 1.4 \text{ mm}^3$  relating to  $13.8 \pm 1.5\%$  at E18.5). As shown previously (SI Appendix Fig. S3C and D), the 2D Lb:Jz ratios showed inter- and intra-sample variations and would benefit from 3D volumetric ratios. The 3D Lb:Jz ratios significantly increased over time due to the expansion of the labyrinth volume, from  $1.76 \pm 0.08$  at E13.5 to  $4.59 \pm 0.45$  at E18.5 (Fig. 4G). Hence, Zr-POM-based CE-CT permitted an initial analysis of placental structures which requires less time compared to standard histology (SI Appendix Table S3).

Comparison of the CE-CT image with the corresponding histological sections revealed that different cell types of the junctional zone could be distinguished (SI Appendix Fig. S3B). Therefore, 3D image analysis was performed on the junctional zone to quantify of the relative proportion of glycogen cells and spongiotrophoblast cells. The volume fraction of glycogen trophoblast cells was at its maximum between E13.5 and E15.5, occupying  $48.5 \pm 1.8\%$  of the junctional zone (Fig. 4H), where after it significantly reduced to  $12.7 \pm 3.4\%$  of the junctional zone near term. In contrast, the volume fraction of the spongiotrophoblasts drastically increased from  $38.9 \pm 3.3\%$  to  $87.4 \pm 3.4\%$ . Notably, lacuna which were evident at earlier stages studied, disappeared from the junctional zone at E15.5 (Fig 3, blue arrows and Fig 4H). These findings indicated that Zr-POM-based CE-CT offers the unique potential to quantify the structure and composition of the junctional zone in 3D, resulting in a more rapid estimation of the junctional zone composition.

#### 4. Zr-POM-based CE-CT to study placental phenotypes and pathologies

##### a. Within species differences in placental development

In biological studies, the C57BL/6J and 129S6 inbred strains are considered the standard laboratory mouse models to study the effect of single gene mutation. However, placental phenotypes and thus embryonic lethality are often strain-dependent, which might prompt backcrossing to the other strain. Remarkably, striking differences exist in the placental morphology between both mouse strains, including the relative distribution of the placental layers (29). To illustrate the validity of Zr-POM-based CE-CT, placentas derived from two different mice strains were compared at different time points of gestation (E14.5 and E18.5) (Fig. 5A). Although fetal weight was similar (Fig. 5B), placental weights were significantly higher by  $\sim 25\%$  at E14.5 and/or E18.5 in C57BL/6J mice compared to 129S6 mice (Fig. 5C). As such, placental efficiency, defined as fetal:placental weight ratios, were

$\sim 10\%$  higher at E14.5 and significantly higher by  $\sim 20\%$  at E18.5 (Fig. 5D). The difference in placental size imposed a different CE-CT scanning resolution of  $3.5 \mu\text{m}$  for 129S6 compared to  $4.5 \mu\text{m}$  for C57BL/6J mice. In line with placental weight, the volume of the C57BL/6J placenta was  $\sim 30\%$  larger at E14.5 and  $\sim 20\%$  at E18.5 (Fig. 5E). While labyrinth volume at E14.5 and E18.5 was similar for 129S6 and C57BL/6J, the volume of the junctional zone was significantly larger in C57BL/6J placentas (Fig. 5F and G). Given the overall smaller placental volume of 129S6 placenta, this difference resulted in an overall altered placental structure regarding volume densities. As such, the volume fraction of the junctional zone at E14.5 and E18.5 of C57BL/6J mice was significantly larger compared to 129S6 mice, whereas the volume fraction of the labyrinth was significantly smaller (Fig. 5G). Consistent with this, visual inspection of the placentas from both strains revealed that the junctional zone of C57BL/6J placentas covered the whole labyrinth until the chorionic plate, whereas the junctional zone was limited to the upper part of the 129S6 placentas (Fig. 5A). Thus, the difference in placental efficiency near term might be attributed to greater proportions of the labyrinth in 129S6 placentas compared to C57BL/6J placentas ( $61.2 \pm 5.1\%$  vs  $45.1 \pm 3.5\%$ , respectively). Nevertheless, at E18.5 placental volume of male and female C57BL/6J fetuses (Fig. 5H). Moreover, volume fractions of the labyrinth and the junctional zone were similar in placentas from male and female fetuses (Fig. 5I).

##### b. Placental phenotype of PI3K mutant mice

To assess whether CE-CT could be used to identify placental defects, the phenotype of the placenta heterozygous deficient in PI3K p110 $\alpha$  was inspected. PI3K p110 $\alpha$  plays a major role in mediating the growth and metabolic effects of the fetoplacental growth factors, insulin and insulin-like growth factors. Homozygous disruption of the p110 $\alpha$  gene results in embryonic lethality, whereas heterozygous disruption ( $\alpha/+$ ) leads to viable pups that are growth restricted near term (30). Recently, the placental phenotypes of  $\alpha/+$  fetuses born from crosses of  $\alpha/+$  males and wild type dams was established using histology and stereology (30). Here, we used CE-CT to validate differences in gross placental morphology observed between  $\alpha/+$  fetuses and wild type littermates at E16 (Fig. 6A). In line with the significant reduction in placental weight described previously (30), the 3D volume of  $\alpha/+$  mutant placentas was significantly less by 15%, compared to wild type littermates ( $74.8 \pm 6.7 \text{ mm}^3$  vs.  $87.6 \pm 6.5 \text{ mm}^3$ ,  $p = 0.0006$ , Fig. 6B and C). Also consistent with previous findings (30),  $\alpha/+$  mutant compared to wild type placentas showed a 20% reduction in the absolute volume of the labyrinth zone ( $27.5 \pm 2.1 \text{ mm}^3$  vs  $34.6 \pm 1.3 \text{ mm}^3$ ,  $p = 0.0004$ ) and no difference in the absolute volume of the junctional zone ( $25.6 \pm 4.3 \text{ mm}^3$  vs.  $25.4 \pm 5.3 \text{ mm}^3$ , Fig. 6D). Consequently, the Lb:Jz ratio was significantly altered in  $\alpha/+$  mutant versus wild type placentas (Fig. 6E). Of note, the volume of the labyrinth zone was  $41.3 \pm 2.9\%$  larger than the junctional zone in wild type littermates, but only  $9.7 \pm 1.8\%$  larger in  $\alpha/+$  placentas. As such, wild type placentas consisted of  $39.7 \pm 3.2\%$  labyrinth and  $28.9 \pm 5.2\%$  junctional zone, whereas  $\alpha/+$  placentas consisted of  $37.2 \pm 2.3\%$  labyrinth and  $34.4 \pm 3.9\%$  junctional zone. Hence,  $\alpha/+$  placentas consist of a significantly larger junctional zone volume fraction. Taken together, our findings validate the use of CE-CT in identifying defects in placental volumes and structure.

#### 5. Additional prospects of Zr-POM-based CE-CT phenotyping of placentas

##### a. Placental vasculature

Interestingly, a very strong contrast was observed for blood inside the fetal and maternal vessels, suggesting that Zr-POM has a high affinity for certain components inside blood. This feature offered the possibility to visualize and analyse properties of blood-filled vessels in intact tissues. Indeed, the 3D images

can be rotated and sectioned in such a way that the diameter of the maternal canals at the junctional-labyrinth border can be measured. Additionally, a thickness distribution of the utero-placental vessels can be assessed, giving an indication of the diameter through the length of the vessel (SI Appendix Fig. S5A). Using this approach, focal haemorrhage spots or ruptures of the vasculature were easily identified (SI Appendix Fig. S5B). Moreover, we found that the diameter of the maternal canal increased by 70% from E13.5 to E17.5 (SI Appendix Fig. S5C and D), which confirmed earlier observations (37). However, the vessels lacking blood and the spatial resolution of 3.5  $\mu\text{m}$ , limited complete separation of fetal and maternal vasculature (SI Appendix Fig. S6) and requires further optimization. Nevertheless, using Zr-POM-based CE-CT, an initial inspection of the utero-placental vasculature can be performed.

#### b. Visualization of placental pathologies

##### i. Embryo resorption

Embryonic resorption is a natural process that occurs in up to 30-40% of the litter (38). Here, we visualized and analysed the placenta from resorbed embryos retrieved at E15.5 and E17.5 of 129S6 mice (Fig. 7A-C). The placenta isolated at E15.5 had a volume of 40.5  $\text{mm}^3$ , of which the labyrinth comprised 44.7% and the junctional zone 21.5%. It therefore had a Lb:Jz - ratio of  $\sim 2$ . These placental volumes however, did not correspond to a typical E15.5 placenta (Fig. 4) and the morphology of the junctional zone was affected (SI Appendix Video S4). In contrast, the placenta of the resorption found at E17.5 showed clear placental defects in the labyrinth, including dilated blood spaces (Fig. 7B). The placental volume was 45.9  $\text{mm}^3$  and consisted of 50.7% labyrinth and 25.7% junctional zone, resulting in a Lb:Jz - ratio of  $\sim 2$  as well. The placental characteristics of the two resorption sites resembled the morphological features that are typical for E14.5 placentas with volumes ranging between 47-53  $\text{mm}^3$ , labyrinth and junctional proportions of 43-55% and 20-29%, respectively, and average ratio values of about 2. These findings might suggest that placental development arrested in both conceptuses around E14.5. Although both fetuses were severely growth restricted, we observed different pathologies in each. In the E15.5 fetus, the resorption was advanced and there were clear signs of degrading tissue apparent in the upper part of the fetal body (SI Appendix Fig. S7A). In contrast, the anatomy of the fetus found at E17.5 was intact, though retarded in development (SI Appendix Fig. S7B). Indeed, both forelimb as hind limb buds were formed but no digits could be distinguished, implying that development halted around Theiler stage 19-20 (corresponding to E11.5-E12.5). These findings exemplified the ease of examining the pathology of embryonic resorptions by Zr-POM-based CE-CT.

##### ii. Mono and dichorionic twin placentas

Fused placentas and twin placentas are rarely observed phenomena in mice. Coincidentally, a fused placenta was retrieved at the cervical pole of an E18.5 C57BL/6J female, with an overall weight of 174 mg (Fig. 7D). Although both embryos retained their own amniotic sac, one fetus was severely growth restricted while the other showed a normal body weight (0.699 g vs 1.05 g). Using CE-CT, the volume fractions of the placental layers were evaluated. Interestingly, the placentas were fused at the junctional zone, suggesting that each fetus retained its own fetoplacental vasculature and this was a di-chorionic, di-amniotic twin pregnancy. However, unequal placental sharing was observed as the growth restricted fetus appropriated only 42% of the placenta. The volume fractions of both parts of the placenta were similar ( $\sim 40\%$  labyrinth and  $\sim 30\%$  junctional zone), suggesting that placentation was not affected per se (Fig. 7F). Although, the small placenta seemingly had more maternal blood pools in the decidua, an increased number of spiral arteries, and more junctional zone inclusions in the labyrinth compared to the larger placenta (SI Appendix Video S5).

In addition, a mono-amniotic twin placenta was retrieved at E18.5 of a C57BL/6J female, in which both embryos resided within one amniotic sac. One fetus had a normal appearance and bodyweight for its gestational age (1.05 g), whereas the other fetus was severely compromised and underdeveloped (bodyweight  $\sim 0.7$  g). The placenta had an overall weight of 191 mg that corresponded to a volume of 140  $\text{mm}^3$ , of which the labyrinth was 70  $\text{mm}^3$  and the junctional zone 43  $\text{mm}^3$ . Notably, two clearly distinguishable insertion sites of the umbilical cord were observed (Fig. 7D and SI Appendix Fig. S8). Although there were pronounced inclusions of the junctional zone within the labyrinth in the middle of the placenta, the separation was not absolute as was observed in the fused placentas, indicating a mono-chorionic twin pregnancy. These findings suggest that the blood supply of the fetuses might have been connected, which may have led to the twin-twin transfusion syndrome. Overall, CE-CT offered the ability to quickly discriminate between placental fusion or mono-amniotic twin placentas.

#### c. Embryonic development

Finally, the anatomy and development of fetuses can be visualized by the incubation of Zr-POM. As such, all vital organs can be inspected and measured in detail, including the lungs, the heart and the liver (SI Appendix Fig. S9 and SI Appendix Video S6). In conclusion, these results suggest that Zr-POM-based CE-CT holds great value to visualize tissue morphology at different stages of the embryonic development, allowing for rapid 3D histology.

## DISCUSSION

New applications for the use of microCT in biomedical sciences are being described constantly. In addition, visualization of soft tissues by diffusion of contrast agents has contributed to its popularity and make microCT very valuable to obtain volumetric data of various tissues. Indeed, CE-CT was recently implemented as a high-throughput tool for morphological analysis of mouse development (26). Although the authors discussed the option to analyse placental development, no quantification of morphological features was performed. However, it was recently described that placental defects are present in almost all mutant strains that die before E14.5 (3), highlighting the importance of inspecting extra-embryonic tissue in new mutant strains. Indeed, failure to appreciate placental defects has resulted in the misconception of gene function during development. Initial analysis of the murine placenta involves measuring the areas of the placental layers on histological sections (11). However, layered structures such as the placenta are prone to anisotropic and non-uniform deformation during tissue processing, which is, withal, a process that is sample specific (39). Quantification of areas on a selected number of slides is therefore merely correct when this is estimated from exhaustive sectioning and stereological analysis. In this study, we validated the use of Zr-POM-based CE-CT as a tool for fast, simple and robust visualization and quantification of the placental morphology.

#### Visualization of placental development

Using Zr-POM-based CE-CT, we were able to image early embryonic development, as well as placentation from E7.5 until term. Indeed, distinct features of the late primitive streak embryo were apparent at E7.5, such as the three cavities, separated by the chorion and the amnion, the ectoplacental cone and the allantoic bud. At E8.5, somite formation and the first signs of chorioallantoic attachment were visible. Therefore, CE-CT could be applied to evaluate whether allantois formation is delayed or whether chorioallantoic attachment occurred. At E9.5, embryo turning and closure of the neural tube could be observed. Interestingly, using our techniques we detected that one embryo imaged was developmentally delayed by one day. In particular, although chorioallantoic fusion had occurred, embryo turning was not complete and somite formation was halted.

953 The definitive mouse placenta and its dynamic changes in  
954 structure could be imaged from E10.5 by Zr-POM-based CE-CT.  
955 Moreover, the structural characteristics of the placenta provided  
956 sufficient contrast to delineate the individual placental layers, as  
957 verified by histology. Indeed, the high correlation between the  
958 area of the labyrinth measured on the CE-CT image and its cor-  
959 responding histological section granted evidence that placental  
960 layers can be delineated by CE-CT to perform volume quantifi-  
961 cation in a straight forward fashion. In addition, we observed large  
962 variations in 2D labyrinth to junctional zone ratios of sections that  
963 were perpendicular, though in the centre of the placenta. Thus,  
964 using intact samples in Zr-POM-based CE-CT offers the distinct  
965 advantage of enabling 3D ratiometric measures that are not prone  
966 to sample bias.

967 Finally, Zr-POM incubation enabled the development of  
968 fetuses to be examined by CE-CT as well. As such, the soft  
969 and mineralized tissues of an E18.5 embryo could be visualized  
970 and allowed the quantification of organs of interest. Obtaining  
971 volumetric measurements of vital organs, such as the brain and  
972 liver, in the fetus offers the additional potential to assess the  
973 symmetry of fetal growth. This is particularly useful as the aetiolo-  
974 gies and perinatal outcomes are believed to vary between fetuses  
975 that are symmetrically versus asymmetrically growth restricted  
976 (40). In addition, this new technique offers the possibility to  
977 explore how placental defects might be associated with fetal organ  
978 development. However, visualization of fetal development by CE-  
979 CT has been described previously (26) and therefore not further  
980 discussed.

#### 981 Quantification of placental development

982 The overall placental volume determined by Zr-POM-based  
983 CE-CT was significantly correlated with placental weight. Placen-  
984 tal density, defined as weight per volume, showed no marked dif-  
985 ferences between the gestational ages studied. Nevertheless, sub-  
986 stantial differences in placental structure between C57BL/6J and  
987 129S6 mice were translated in altered density values. Therefore,  
988 calculating this parameter might be useful in identifying where  
989 there may be a disconnection between placental growth and  
990 structural changes in pathological mouse pregnancies. Moreover,  
991 measurements of placental density in human placentas could be  
992 used to predict pregnancy complications before delivery, assum-  
993 ing volume and weight measurements from ultrasound (41).

994 In line with stereological assessments of the C57BL/6J pla-  
995 centa (9), the absolute volume and volume fraction of the pla-  
996 cental labyrinth zone determined by Zr-POM-based CE-CT also  
997 increased towards term in 129S6 placentas. These ontogenic  
998 changes are also consistent with the increasing demands for  
999 nutrient exchange by the placenta to cope with exponential fetal  
1000 growth. On the contrary, the absolute and fractional volumes of  
1001 the junctional zone and decidua decreased over time. Attaining  
1002 volume quantities of the placental layers by Zr-POM-based CE-  
1003 CT provided the possibility to determine the true 3D labyrinth  
1004 to junctional zone ratio, which was not section-dependent. More-  
1005 over, other morphological features of the placental layers could  
1006 also be visualized with Zr-POM-based CE-CT. In particular, the  
1007 proportion of glycogen cells and spongiotrophoblast cells in the  
1008 junctional zone could be evaluated because of the difference in  
1009 cellular composition. This presents the opportunity to assess the  
1010 volume of glycogen cells in cases of placental hypo/hyperplasia  
1011 or in complicated pregnancies such as gestational diabetes mel-  
1012 litus and intrauterine growth restriction (42). Similar to what is  
1013 described in previous studies (33), the amount of glycogen cells  
1014 residing in the junctional zone decreased significantly towards  
1015 term. Although the migration of the glycogen into the maternal  
1016 decidua could not be readily visualized, defects in migration may  
1017 be indirectly inferred if more glycogen cells were resident within  
1018 the junctional zone. Additionally, this research tool offers the  
1019 opportunity to quantify ectopic inclusions of the junctional zone

1020 in the labyrinth, in terms of number, size and cellular composi-  
1021 tion. Indeed, observing an increased abundance of these ectopic  
1022 inclusions in the labyrinth may reflect defects in placental devel-  
1023 opment (34). However, secondary trophoblast giant cells, which  
1024 compose an additional cell population of the junctional zone were  
1025 not identifiable. In contrast, primary trophoblast giant cell layer  
1026 enclosing the conceptus at E8.5 were distinguishable from the  
1027 surrounding decidua. As this study was the first to describe CE-  
1028 CT to assess placental morphology through multi-tissue visualiza-  
1029 tion, it would benefit from further optimization. Most likely, the  
1030 standard image processing algorithms used in this study are not  
1031 sufficient to acquire all information from the images and more  
1032 advanced techniques, such as machine or deep learning, could  
1033 result in more accurate quantifications. In addition, comparing  
1034 the CE-CT images with corresponding histological sections of  
1035 the same sample required detailed comparison and interpolation  
1036 of the CE-CT dataset. One method to overcome this may be  
1037 to subject the CE-CT-imaged samples to further processing by  
1038 tissue clarification and immune-labelling. Using this approach,  
1039 3D constructions of CE-CT-scanned sample could be compared  
1040 to the 3D construction of the immune-labelled cleared sample  
1041 (43, 44).

1042 Critical to fetal survival is the reciprocal exchange of gases,  
1043 nutrients and waste between mother and fetus. Spiral arteries  
1044 from the maternal decidua coalesce at the border of the junctional  
1045 zone into one to four central canals that shunt maternal blood to  
1046 the bottom of the labyrinth. The oxygen-poor fetal blood flows via  
1047 arterioles into labyrinth where they extensively branch into dense  
1048 capillaries, which drain the oxygen-rich blood back towards the  
1049 fetus. In mice, the maternal blood is separated from fetal blood by  
1050 a trilaminar interhaemal membrane that comprises fetal endothe-  
1051 lial cells and two syncytiotrophoblast layers. Here, the affinity  
1052 of Zr-POM for blood enabled the visualization of the placental  
1053 vasculature in CE-CT without additional intravascular infusion  
1054 of contrast agents. In particular, we observed that the diameter  
1055 of the uterine canals increased from E13.5 to E17.5, which is in  
1056 line with previous reports (37). Additionally, focal haemorrhage  
1057 could also be easily detected. Disadvantageously, the visualization  
1058 of blood vessels depended on blood to be retained within the  
1059 vessels. Moreover, the spatial resolution in this study (3.5  $\mu\text{m}$ ) was  
1060 insufficient to completely separate the two vasculatures since the  
1061 minimum thickness of the interhaemal membrane is 4.8  $\mu\text{m}$  near  
1062 term (10). Thus, additional work is required to optimize the image  
1063 analysis software to allow accurate assessment of the labyrinth  
1064 exchange interface. Nevertheless, detailed analysis of the utero-  
1065 and fetoplacental vasculature has been described previously by  
1066 the use of intravenous contrast agents in mouse and human  
1067 placentas (45). Although these methods can be used to obtain  
1068 hemodynamic insights, capillaries cannot be visualized and in-  
1069 formation on the basic placental morphology cannot be attained.  
1070 Therefore, it might be promising to combine intravenous applied  
1071 contrast agent to stain larger blood vessels and Zr-POM to vi-  
1072 sualize morphology and the residual blood within the capillaries.  
1073 Alternatively, optimizing sample preparation for Zr-POM-based  
1074 CE-CT such that the placental vessels remain filled with blood,  
1075 may improve branching analysis. Although not assessed in this  
1076 study, this feature may also be exploited to assess the extent of  
1077 spiral artery remodelling at the fetomaternal interface, as this is  
1078 an important for successful pregnancy.

#### 1079 Biological and genetic variation of placentas

1080 The 129S6 and C57BL/6J mice are the two most popu-  
1081 lar mouse strains used in laboratories. Interestingly, embryonic  
1082 lethality and placental defects are often strain dependent. Here,  
1083 we exploited the fact that genetic background affects placen-  
1084 tal morphology to validate the ability of Zr-POM-based CE-  
1085 CT to quantify placental volumes (29). In line with literature,  
1086 we observed significantly larger placental volume, as well as an  
1087  
1088

increased volume fraction of the junctional zone but a decreased labyrinth volume fraction in C57BL/6J mice compared to 129S6 using CE-CT. This significantly smaller exchange surface might explain the reduced placental efficiency of C57BL/6J placentas and might impose a more severe phenotype in mutants that affect labyrinth functioning. Recently, sexual dimorphic differences in placental phenotypes are being described (46, 47). This area still being in its infancy, it remains unclear whether placental volume fractions are different in placentas from wild type male and female fetuses. In this study, no differences were observed in either placental volume or volume fraction at E18.5 placentas from C57BL/6J mice. These findings are in line with stereological assessments of rat placentas where sexual dimorphic differences observed at midgestation were no longer present at E20 (48). These findings confirm the striking difference in placental morphology between mouse strains and validate the use of the Zr-POM CE-CT methodology.

In addition, the use of Zr-POM-based CE-CT to detect placental defects was assessed in a model with known placental malfunction. Pups that are heterozygous deficient for the PI3K isoform, p110 $\alpha$  ( $\alpha$ +) are growth restricted as a result of a smaller placenta and defective labyrinth zone formation (30). Consistent with this, we also observed significantly smaller placental volumes and a reduced labyrinth volume in  $\alpha$ /+ mutants compared to wild type littermates using the CE-CT technique. These findings would prompt a detailed inspection of the labyrinth exchange region. Indeed, using stereology, the authors showed that fetal capillary volume and length, exchange surface area and diffusion capacity were all decreased in  $\alpha$ /+ mutants (30).

Apart from differences between different mouse strains, striking variations were also observed in naturally occurring resorption sites. Placental volumes were analysed from placentas of resorbed conceptuses, which were severely growth restricted and demised at E15.5 and E17.5. Interestingly, both placentas had structural characteristics that resembled E14.5 placentas, suggesting that placental development did not progress past E14.5. Impaired junctional morphology was observed in the E15.5 placenta and embryonic resorption was clearly ongoing. In contrast, the placenta isolated at E17.5 had dilated blood spaces in the labyrinth and disturbed placental morphology, since the volume fraction of the labyrinth was reduced compared to a normal E17.5 placenta. These findings might indicate that proper functioning of both the labyrinth, as well as the junctional zone are important for normal development.

Fusion of placentas from neighbouring embryos is a rare phenomenon with an estimated frequency of less than 1%. It is thought to result from aberrant embryo spacing or overcrowding, which leads to competition for nutrients and space between neighbouring conceptuses, and ultimately, impaired fetal development (49, 50). We examined a fused placenta of two conceptuses by Zr-POM-based CE-CT, one having a normal fetal weight for an E18.5 embryo, while the other was severely growth restricted (being 50% smaller). Given the advantage of CE-CT to obtain 3D histological data, the morphology of the fused placentas could be easily examined. Interestingly, each conceptus retained their own labyrinth, whereas the junctional zones were fused in the middle. This implied that the growth restriction of the small conceptus was not caused by unbalanced blood flow from one fetus to the other. Nevertheless, we did observe a disproportionate distribution of the placental mass with the normally growing fetus supported by 58% of the fused placenta. Moreover, the volumes of the labyrinth and the junctional zone were higher for the normal weight fetus. However, the volume fractions of the placental regions were very similar between the normal weight and growth restricted fetus, resulting in similar zonal ratios. These findings suggest that placentation per se was not affected, but competition for space and nutrients impacted normal placental

growth and thus fetal growth. Interestingly, there were many large blood vessels in the maternal decidua covering the smaller of the fused placentas. This may reflect an attempt of the mother to compensate and increase resource supply to the conceptus, which although, was insufficient to maintain normal growth.

Finally, we observed a placenta with two umbilical cords and a labyrinth that was seemingly not separated per fetus. This could imply that fetal blood supplies were connected, which posed a risk of unbalanced blood flow and might result in twin-twin transfusion syndrome. Although our current analyses were unable to identify vessels that linked the blood flow between the twins, one twin suffered from poor nourishment and hence fetal demise.

Taken together, this study illustrated for the first time the use of Zr-POM-based CE-CT to assess mouse placental development and its most common defects, including failure of chorioallantoic attachment, a small placenta, distorted placental structure, junctional zone inclusions in the labyrinth, underdeveloped labyrinth, disorganized junctional zone, the presence of fibrotic or necrotic areas and dilated blood spaces. Indeed, CE-CT offers a non-destructive, quantitative and robust technique to evaluate, within one dataset, different placental parameters like the total volume, volume fractions, ratio of different placental layers and volumes of specific cell populations. Moreover, this research tool allows the inspection of the vasculature within the entire placenta, as well as identifying placental defects in embryonic resorption and placental fusion pathologies. Collectively, the possibility of multi-sample holders, in addition to the ease of the technique and the high spatial resolution, render Zr-POM-based CE-CT as a promising tool that can be automated for high-throughput screening of structural defects. Indeed, Zr-POM-based CE-CT offers the advantage to inspect the 3D structure of the placenta and has an immense complementary value to histology

## MATERIALS AND METHODS

### Mice

All animal experiments were approved by the Ethical Committee of the Faculty of Biomedical Sciences of the KU Leuven. They were housed in filter-top cages under conventional conditions and kept under controlled conditions. 8 to 12-week-old 129S6 inbred mice were obtained from an internal breeding program. C57BL/6J inbred mice were obtained from Janvier (France). The PI3K p110 $\alpha$  mice were bred in the University of Cambridge Animal Facility abiding by the UK Home Office Animals (Scientific Procedures) Act 1986 and local ethics committee and genotyping was performed as previously described (30). Mice were mated and the detection of a copulation plug was dated as E0.5 of pregnancy. Unless mentioned otherwise, samples were isolated, fixed in 4% PFA for 24 hours and stored in Dulbecco's Phosphate-buffered saline (DPBS, Gibco, Belgium). Placentas from E10.5 and E11.5 were isolated with the mesometrial triangle. For the visualization of the early development, implantation sites from E7.5-E9.5 were isolated within the myometrium and decidual tissue. Fetuses of E18.5 were euthanized by intraperitoneal injection of ketamine/xylazine (300mg/kg + 30mg/kg), fixed in 4%PFA for 48h and stored in DPBS. Small slices were made in the skin to improve diffusion of the contrast agent. Only animals with litters of more than four fetuses were included in the study.

### Contrast-enhanced CT

#### Contrast agent

The contrast agent used was a Zirconium-substituted Keggin polyoxometalate (51):  $((\text{Et}_2\text{NH}_2)_{10}[\text{Zr}(\text{PW}_{11}\text{O}_{39})_2] \cdot 7\text{H}_2\text{O})$ . The Zr-POM has a net charge of -10 (the metal ion +4 and the polyoxometalate -14) and a molecular weight of 6313.43 g/mol. Placental samples were incubated for at least 7 days, and fetuses for 28 days, in the contrast solution (35mg per ml PBS), while gently shaking (50 rpm) at room temperature.

#### CE-CT - acquisition

Placentas were scanned in PBS using a Phoenix Nanotom M (GE Measurement and Control Solutions, Germany) at 3.5  $\mu\text{m}$  (129S6) or 4.5  $\mu\text{m}$  (C57BL/6J) isotropic voxel size. The source, equipped with a tungsten target, was operated at 60 kV and 240  $\mu\text{A}$ . An aluminium filter of 0.1 mm was applied to reduce beam hardening. For each sample, 2400 frames were acquired over 360° using the fast scan mode with an exposure time of 500 ms (frame averaging = 1 and image skip = 0) (25), resulting in a scanning time of only 20 minutes per sample.

Fetuses were scanned in PBS at 7 $\mu\text{m}$  isotropic voxel size at 60 kV and 300 $\mu\text{A}$ , using a 0.2mm aluminium filter. To visualize the complete fetus, a multiscan approach was applied. For each scan, 1800 frames were acquired over 360° with an exposure time of 500ms (frame averaging = 3 and image skip = 1), resulting in a total scan time of 2hrs45min.

1225 Afterwards, scan optimization (projection filter, inline volume filter, and  
1226 beam hardening correction) was applied during 3D reconstruction (Datos|x,  
1227 GE Measurement and Control solutions).

#### 1228 Data display and statistics

1229 Graph display and statistics were done in Graphpad Prism (Graphpad  
1230 Software, USA). Normality was assessed with D'agostino & Pearson omnibus  
1231 normality test. Data were analysed with Mann-Whitney test, Kruskal-Wallis  
1232 multiple comparison test with Dunn's corrections or Two-way ANOVA test  
1233 with Dunnett's corrections. Correlations were tested with Pearson correlation  
1234 test or the nonparametric Spearman correlation test. Differences were con-  
1235 sidered statistically significant when  $p < 0.05$ . Boxplots displayed median with  
1236 1<sup>st</sup> and 3<sup>rd</sup> quartile with whiskers at the minimum and maximum values. Data

1. Ayadi A, et al. (2012) Mouse large-scale phenotyping initiatives: overview of the European Mouse Disease Clinic (EUMODIC) and of the Wellcome Trust Sanger Institute Mouse Genetics Project. *Mamm Genome* 23(9-10):600-610.
2. Dickinson ME, et al. (2016) High-throughput discovery of novel developmental phenotypes. *Nature* 537(7621):508-514.
3. Perez-Garcia V, et al. (2018) Placentation defects are highly prevalent in embryonic lethal mouse mutants. *Nature* 555(7697):463-468.
4. Camm EJ, Botting KJ, & Sferruzzi-Perri AN (2018) Near to One's Heart: The Intimate Relationship Between the Placenta and Fetal Heart. *Front Physiol* 9:629.
5. Barker DJ, Osmond C, Golding J, Kuh D, & Wadsworth ME (1989) Growth in utero, blood pressure in childhood and adult life, and mortality from cardiovascular disease. *BMJ* 298(6673):564-567.
6. Vaag AA, Grunnet LG, Arora GP, & Brons C (2012) The thrifty phenotype hypothesis revisited. *Diabetologia* 55(8):2085-2088.
7. Napso T, Yong HEJ, Lopez-Tello J, & Sferruzzi-Perri AN (2018) The Role of Placental Hormones in Mediating Maternal Adaptations to Support Pregnancy and Lactation. *Front Physiol* 9:1091.
8. Rossant J & Cross JC (2001) Placental development: lessons from mouse mutants. *Nat Rev Genet* 2(7):538-548.
9. Coan PM, Ferguson-Smith AC, & Burton GJ (2004) Developmental dynamics of the definitive mouse placenta assessed by stereology. *Biol Reprod* 70(6):1806-1813.
10. Coan PM, Ferguson-Smith AC, & Burton GJ (2005) Ultrastructural changes in the interhaemal membrane and junctional zone of the murine chorioallantoic placenta across gestation. *J Anat* 207(6):783-796.
11. Natale DR, Starovic M, & Cross JC (2006) Phenotypic analysis of the mouse placenta. *Methods Mol Med* 121:275-293.
12. Howard CV & Reed M (1998) Volume and surface-area estimation from microscopic images. *J Microsc-Oxford* 190:291-291.
13. Gundersen HJ & Jensen EB (1987) The efficiency of systematic sampling in stereology and its prediction. *J Microsc* 147(Pt 3):229-263.
14. Mayhew TM & Burton GJ (1997) Stereology and its impact on our understanding of human placental functional morphology. *Microsc Res Tech* 38(1-2):195-205.
15. Kallai I, et al. (2011) Microcomputed tomography-based structural analysis of various bone tissue regeneration models. *Nature protocols* 6(1):105-110.
16. Bouxsein ML, et al. (2010) Guidelines for assessment of bone microstructure in rodents using micro-computed tomography. *Journal of bone and mineral research : the official journal of the American Society for Bone and Mineral Research* 25(7):1468-1486.
17. Marxen M, et al. (2004) MicroCT scanner performance and considerations for vascular specimen imaging. *Med Phys* 31(2):305-313.
18. Chi L, et al. (2017) G9a controls placental vascular maturation by activating the Notch Pathway. *Development* 144(11):1976-1987.
19. Rai A & Cross JC (2014) Development of the hemochorial maternal vascular spaces in the placenta through endothelial and vasculogenic mimicry. *Dev Biol* 387(2):131-141.
20. Rennie MY, Rahman A, Whiteley KJ, Sled JG, & Adamson SL (2015) Site-specific increases in utero- and fetoplacental arterial vascular resistance in eNOS-deficient mice due to impaired arterial enlargement. *Biol Reprod* 92(2):48.
21. Rennie MY, et al. (2011) Vessel tortuosity and reduced vascularization in the fetoplacental arterial tree after maternal exposure to polycyclic aromatic hydrocarbons. *Am J Physiol Heart Circ Physiol* 300(2):H675-684.
22. Zhou YJ, Yuan ML, Li R, Zhu LP, & Chen ZH (2013) Real-time placental perfusion on contrast-enhanced ultrasound and parametric imaging analysis in rats at different gestation time and different portions of placenta. *PLoS One* 8(4):e58986.
23. Langheinrich AC, et al. (2008) Quantitative 3D micro-CT imaging of the human fetoplacental vasculature in intrauterine growth restriction. *Placenta* 29(11):937-941.
24. Junaid TO, Bradley RS, Lewis RM, Aplin JD, & Johnstone ED (2017) Whole organ vascular casting and microCT examination of the human placental vascular tree reveals novel alterations associated with pregnancy disease. *Sci Rep* 7(1):4144.
25. Kerckhofs G, et al. (2016) Changes in bone macro- and microstructure in diabetic obese mice revealed by high resolution microfocus X-ray computed tomography. *Sci Rep* 6:35517.
26. Hsu CW, et al. (2016) Three-dimensional microCT imaging of mouse development from early post-implantation to early postnatal stages. *Dev Biol* 419(2):229-236.

display and 3D rendering of the CE-CT images was done by Dataviewer and CTvox (Bruker MicroCT).

#### ACKNOWLEDGEMENTS

JV, KDC and EP acknowledge the Research Foundation - Flanders (FWO/1122215N, GOD1417N and GOA6719N). The CE-CT images were generated at the X-ray CT facilities of the Department of Development and Regeneration (KU Leuven), financed by the Hercules Foundation (AKUL 13/47). ANSP acknowledges the Royal Society for a Dorothy Hodgkin Research Fellowship and Academy of Medical Sciences for a Springboard Grant and TN acknowledges the ERC for a Marie Curie International Fellowship. Conflicts of interest: none

27. Kerckhofs G, et al. (2018) Simultaneous three-dimensional visualization of mineralized and soft skeletal tissues by a novel microCT contrast agent with polyoxometalate structure. *Biomaterials* 159:1-12.
28. Buytaert J, Goyens J, De Greef D, Aerts P, & Dirckx J (2014) Volume Shrinkage of Bone, Brain and Muscle Tissue in Sample Preparation for Micro-CT and Light Sheet Fluorescence Microscopy (LSFM). *Microsc Microanal* 20(4):1208-1217.
29. Tunster SJ, Van de Pette M, & John RM (2012) Impact of genetic background on placental glycogen storage in mice. *Placenta* 33(2):124-127.
30. Sferruzzi-Perri AN, Lopez-Tello J, Fowden AL, & Constanica M (2016) Maternal and fetal genomes interplay through phosphoinositol 3-kinase(PI3K)-p110alpha signaling to modify placental resource allocation. *Proc Natl Acad Sci U S A* 113(40):11255-11260.
31. Armit C, et al. (2017) eMouseAtlas: An atlas-based resource for understanding mammalian embryogenesis. *Dev Biol* 423(1):1-11.
32. Kerckhofs G, et al. (2017) Simultaneous three-dimensional visualization of mineralized and soft skeletal tissues by a novel microCT contrast agent with polyoxometalate structure. *Biomaterials* 159:1-12.
33. Coan PM, Conroy N, Burton GJ, & Ferguson-Smith AC (2006) Origin and characteristics of glycogen cells in the developing murine placenta. *Dev Dyn* 235(12):3280-3294.
34. Rampon C, et al. (2008) Protocadherin 12 deficiency alters morphogenesis and transcriptional profile of the placenta. *Physiol Genomics* 34(2):193-204.
35. Adamson SL, et al. (2002) Interactions between trophoblast cells and the maternal and fetal circulation in the mouse placenta. *Dev Biol* 250(2):358-373.
36. Simmons DG (2014) Postimplantation development of the chorioallantoic placenta. *The guide to investigate mouse pregnancy*, ed Croy BAY, A.T; DeMayo F.J; Adamson, S.L. (Elsevier).
37. Yadav BK, et al. (2016) A longitudinal study of placental perfusion using dynamic contrast enhanced magnetic resonance imaging in murine pregnancy. *Placenta* 43:90-97.
38. Flores LE, Hildebrandt TB, Kuhl AA, & Drews B (2014) Early detection and staging of spontaneous embryo resorption by ultrasound biomicroscopy in murine pregnancy. *Reprod Biol Endocrinol* 12:38.
39. Dorph-Petersen KA, Nyegaard JR, & Gundersen HJ (2001) Tissue shrinkage and unbiased stereological estimation of particle number and size. *J Microsc* 204(Pt 3):232-246.
40. Dashe JS, McIntire DD, Lucas MJ, & Leveno KJ (2000) Effects of symmetric and asymmetric fetal growth on pregnancy outcomes. *Obstet Gynecol* 96(3):321-327.
41. Kim HS, Cho SH, Kwon HS, Sohn IS, & Hwang HS (2014) The significance of placental ratios in pregnancies complicated by small for gestational age, preeclampsia, and gestational diabetes mellitus. *Obstet Gynecol Sci* 57(5):358-366.
42. Akison LK, Nitert MD, Clifton VL, Moritz KM, & Simmons DG (2017) Review: Alterations in placental glycogen deposition in complicated pregnancies: Current preclinical and clinical evidence. *Placenta* 54:52-58.
43. Merz G, Schwenk V, Shah RG, Necaie P, & Salafia CM (2017) Clarification and 3-D visualization of immunolabeled human placenta villi. *Placenta* 53:36-39.
44. Kagami K, Shinmyo Y, Ono M, Kawasaki H, & Fujiwara H (2017) Three-dimensional visualization of intrauterine conceptus through the uterine wall by tissue clearing method. *Sci Rep* 7(1):5964.
45. Rennie MY, Whiteley KJ, Kulandavelu S, Adamson SL, & Sled JG (2007) 3D visualisation and quantification by microcomputed tomography of late gestational changes in the arterial and venous fetoplacental vasculature of the mouse. *Placenta* 28(8-9):833-840.
46. Wiczorek A, et al. (2019) Sex-specific regulation of stress-induced fetal glucocorticoid surge by the mouse placenta. *Am J Physiol Endocrinol Metab*.
47. Kalisch-Smith JI, Simmons DG, Dickinson H, & Moritz KM (2017) Review: Sexual dimorphism in the formation, function and adaptation of the placenta. *Placenta* 54:10-16.
48. Kalisch-Smith JI, Simmons DG, Pantaleon M, & Moritz KM (2017) Sex differences in rat placental development: from pre-implantation to late gestation. *Biol Sex Differ* 8:17.
49. Chen Q, et al. (2011) Transient {beta}2-adrenoceptor activation confers pregnancy loss by disrupting embryo spacing at implantation. *J Biol Chem* 286(6):4349-4356.
50. Carr JG (1946) Placental fusion in mice. *Proc R Soc Edinb Biol* 62(2):189.
51. Ly HGT & Parac-Vogt TN (2017) Spectroscopic Study of the Interaction between Horse Heart Myoglobin and Zirconium(IV)-Substituted Polyoxometalates as Artificial Proteases. *Chemphyschem* 18(18):2451-2458.